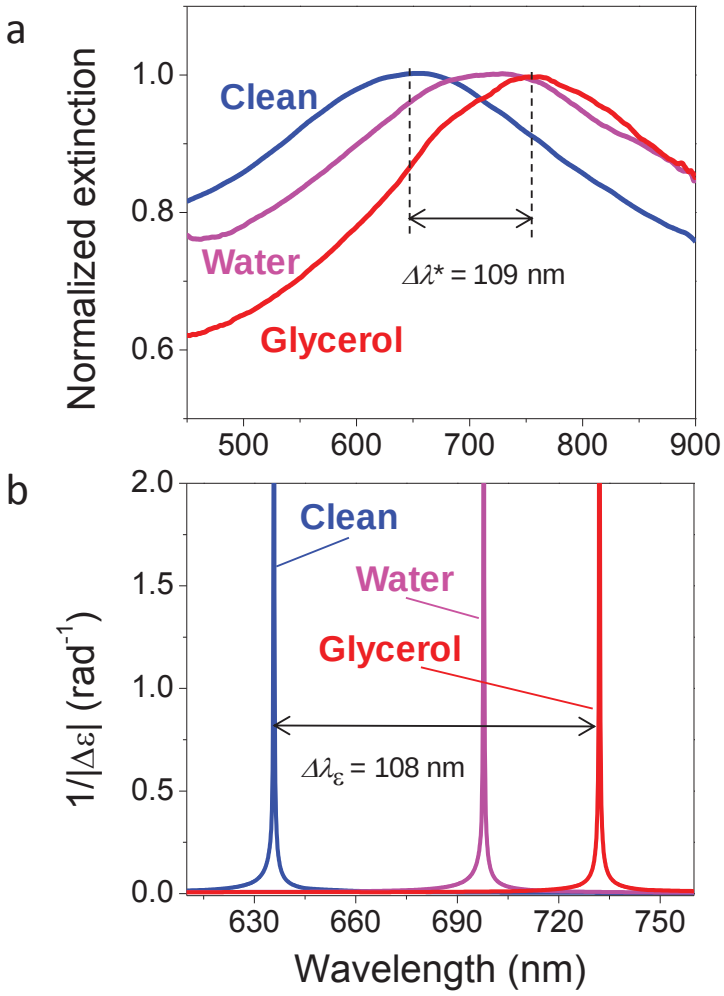

Supplementary Figure 1. Refractive index sensitivity of Ni magnetoplasmonic nanoantennas. **a** Extinction spectra of Ni cylindrical nano-antennas with lateral dimensions of 160 ± 5 nm (diameter) and 30 nm (thickness) for different values of the embedding refractive index (clean n=1, water n=1.33, and glycerol n=1.47). The wavelength shift Δλ*of the resonance peak is 109 ± 15 nm after a refractive index change Δn of 0.47. **b** Plot of the inverse of transmitted light ellipticity variation 1/|$\Delta\varepsilon$| for the same values of the embedding refractive index as above. The shift of the wavelength at which 1/| $\Delta\varepsilon$| resonates is 108 ± 0.25nm.

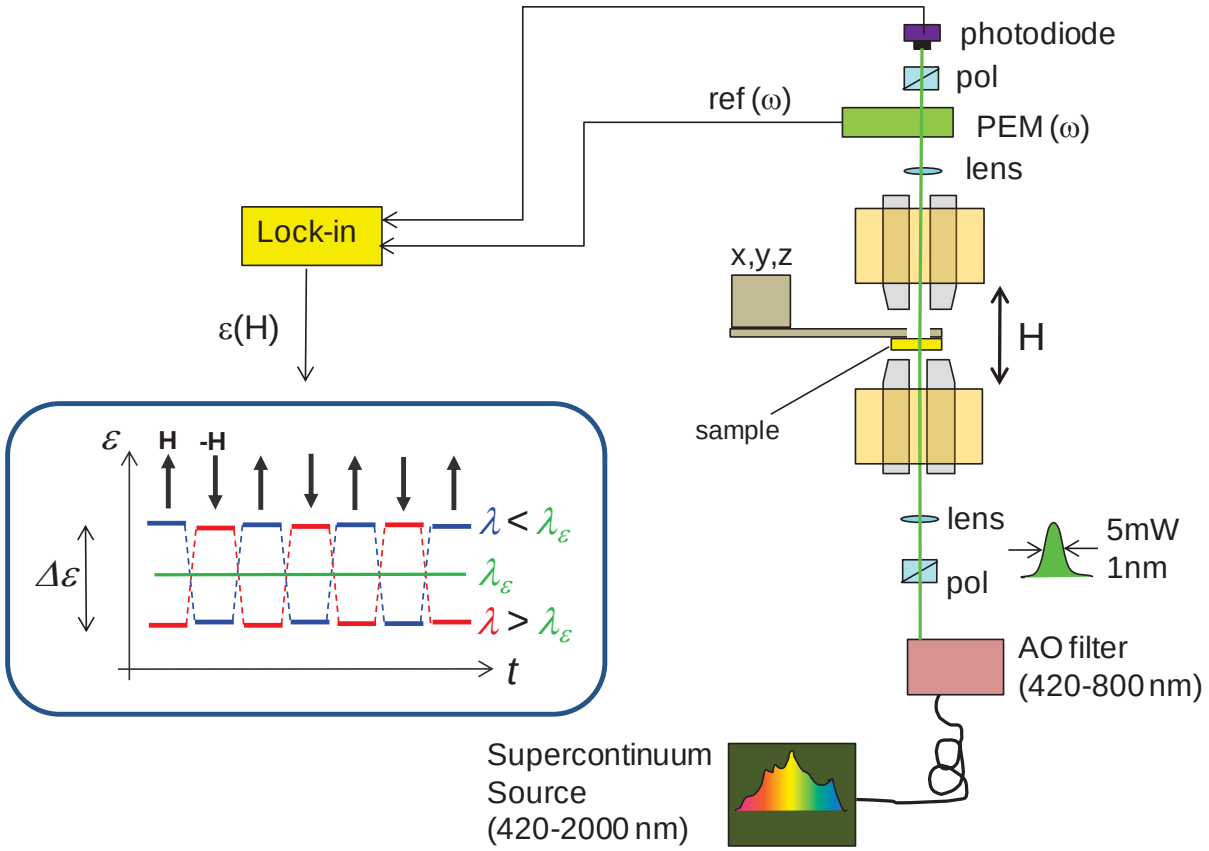

Supplementary Figure 2. Schematic of the experimental setup utilized for measuring $\Delta\varepsilon(\lambda)$. A ultra-broadband supercontinuum radiation source (Fianium model®) is coupled via a multimode optical fiber to an acousto-optic tunable filter (AO filter) to get monochromatic light in the wavelengths range 420-950 nm, with a resolution of 1 nm. The light beam is linearly polarized passing through a Glann-Thompson polarizer and then is focused on to the sample surface and perpendicular to it via a lens with a 500 mm focal length. The sample is placed in the gap of an electromagnet, whose poles have a conical bore (entrance diameter 10 mm and exit diameter 4 mm). The transmitted or reflected light is then collected by a lens with equal focal length as the focusing one and directed to the detection system (only the transmission case is shown in Figure for simplicity; in reflection experiments the laser beam is sent at 2 degrees from the perpendicular to the sample surface). At each wavelength we induced the magneto-optical activity in the Ni nanoantennas by magnetically saturating them along two opposite directions perpendicular to the sample surface by applying an external field H ~ 4 kOe. The detection system implements the so called polarization modulation technique[1] and is constituted by a photoelastic modulator (PEM) operated at a frequency ω = 50 kHz followed by a polarizer oriented at 5 degrees from extinction, viz., with its polarization axis at 85 degrees from that of the first polarizer, and a Si photodetector eventually detects the intensity of the transmitted light. The ellipticity ε of the transmitted light induced by H is determined by filtering out the ω component of the photedector signal using a lock-in amplifiers. In our experiments we measure the ellipticity variation $\Delta\varepsilon = \varepsilon(H) - \varepsilon(-H)$ at each wavelength λ by switching back and forth the saturating field H, as sketched in the inset. $\Delta\varepsilon = 0$ at the null wavelength λ_ε.

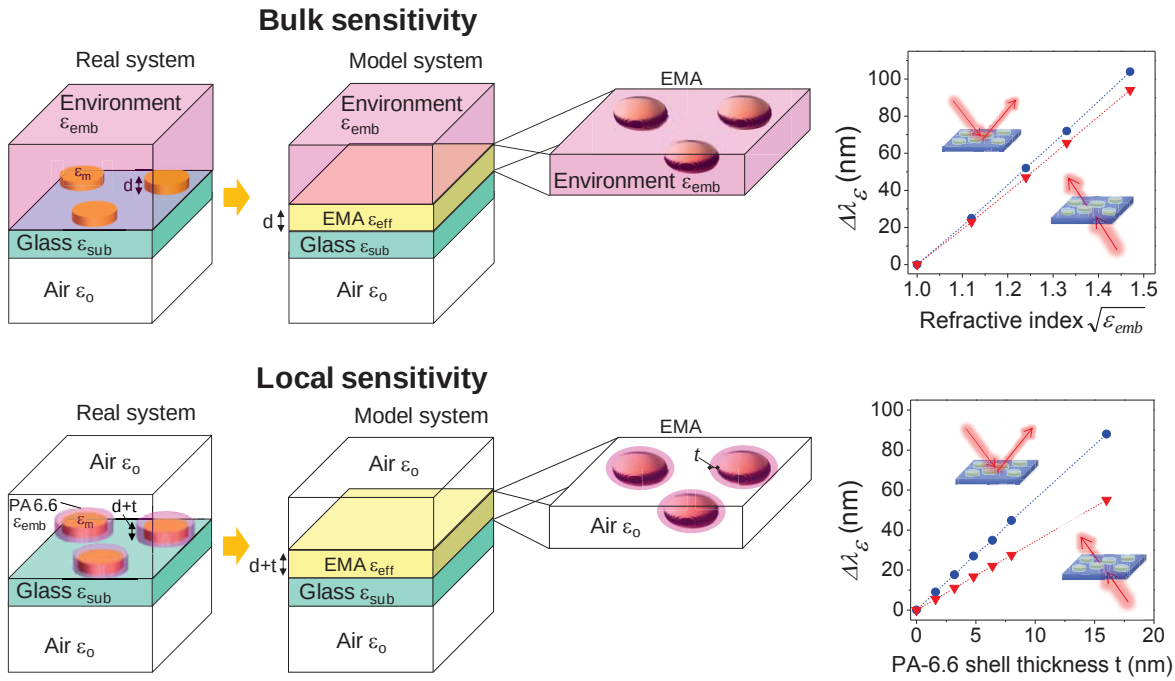

Supplementary Figure 3. Simulations of ε null-point shift for bulk and local sensitivity. As discussed in the main text and in the previous Supplementary Figure 3, Δε can be equivalently measured in reflection geometry. A comparison between bulk refractive index sensitivity experiments conducted in the both transmission and reflection geometry (not shown) show a very similar bulk refractive index sensitivity $S_{RI} = \Delta\lambda_\varepsilon/\Delta n$. On the other hand, local refractive index experiments as those shown in Figures 3 and 4, show the remarkable boosting by a factor 1.7 in the surface sensitivity $S_{Surf} = \Delta\lambda_\varepsilon/\Delta t$ of reflection experiments as compared to transmission ones. Such boosting effect in S_{Surf} makes the reflection geometry more appealing for local sensitivity applications also because the detection can be done with the light probe coming from the substrate side, as in the schematic of a simplified setup shown in the Supplementary Figure S6. The enhancement of S_{Surf} in reflection is due to the additional phase contribution of *uncovered* glass substrate (ε_{sub}) reflectivity to determine the polarization of the reflected light. In order to prove this, we performed calculations using an approach based on the computation of the polarizability of a single ferromagnetic nanoantenna (dielectric tensor ε_m) approximated by a flat ellipsoid of revolution[2]. The assembly of nanoantennas in the external environment (ε_{eff}) is then modeled as a layer with an effective dielectric tensor ε_{eff} calculated using a standard effective medium approximation (EMA). The far-field polarization if eventually calculated modeling the complete system as a bilayer EMA/Glass applying the Transfer Matrix Method (TMM)[2]. The upper panel of the Figure shows the bilayer system we have used to simulate the bulk sensitivity experiments, both in transmission and in reflection geometry. The case of local sensitivity experiments is shown in the bottom panel. In this latter case, the nanoantennas are modeled as core-shell ellipsoids, with the shell of variable thickness *t* made of PA-6.6. The right-hand panels show the results of simulations that confirm the boosting effect observed in local sensitivity experiments conducted in reflection geometry. The calculations yield a boosting factor of 1.65 which is in excellent agreement with the value of 1.7 found experimentally.

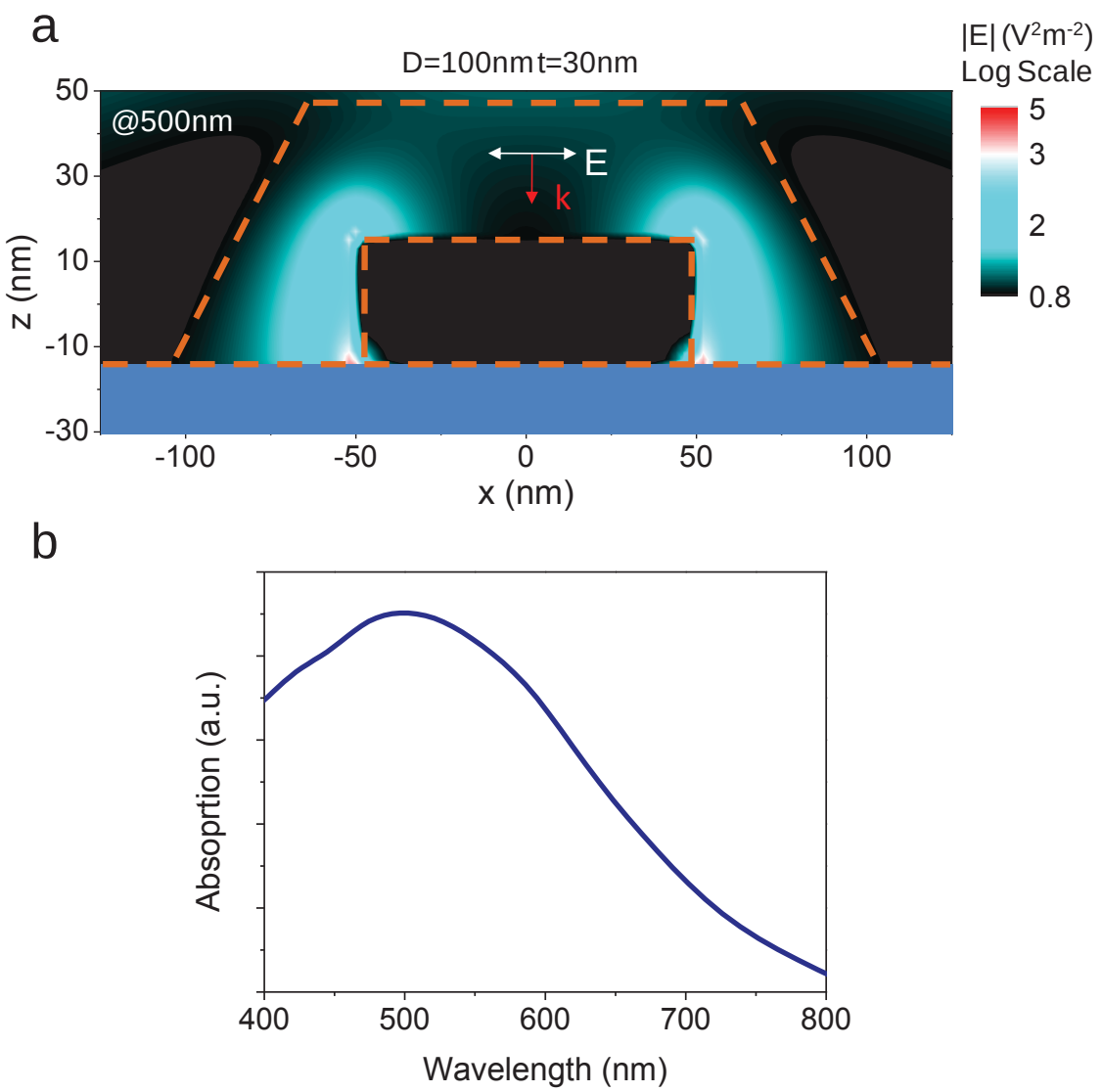

Supplementary Figure 4. Finite Difference Time Domain (FDTD) simulations. a Near field amplitude |E| of a Ni nanodisk on glass with diameter D and thicknes t of 100 nm and 30 nm, respectively. The simulated area is in the X-Z plane at the center of the nanodisk. The wavelength of the incident field is 500 nm. As highlighted by the orange dashed-line the near-field profile has a spatial extension of ~35 nm. The light blue bar under the disk is the substrate. **b** Corresponding calculated absorption cross section (the black dashed-line indicates the wavelength at which the near-field profile is simulated).

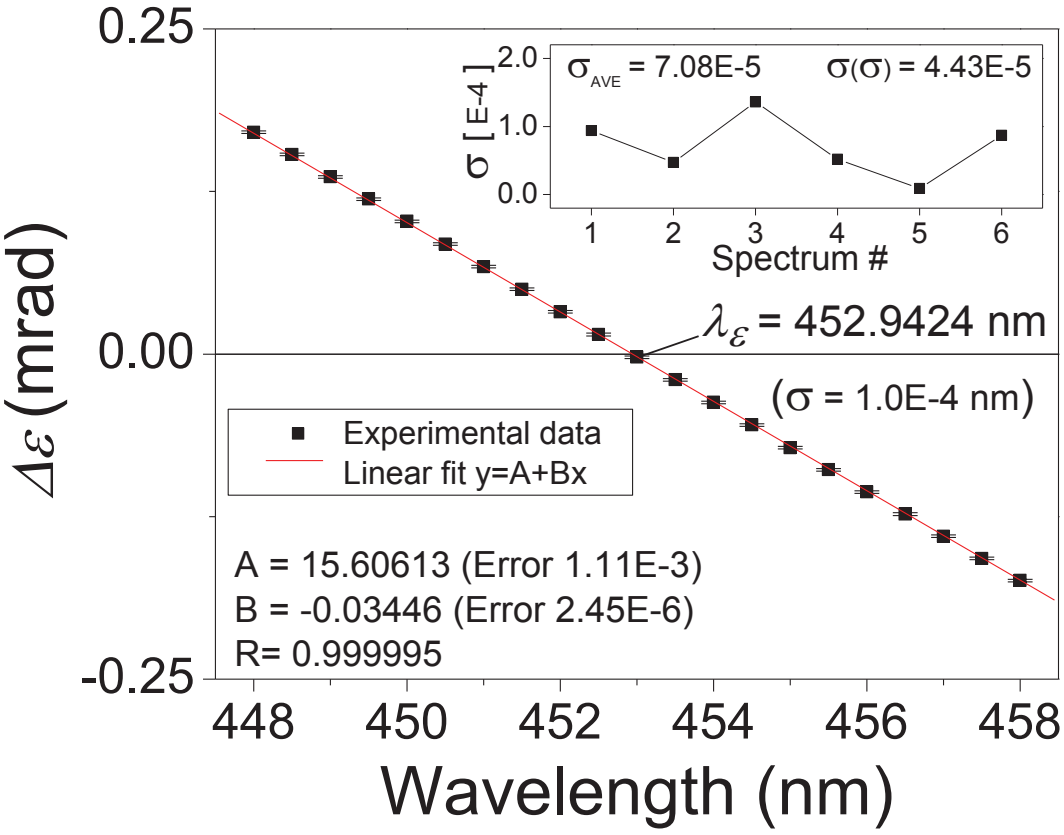

Supplementary Figure 5. Sensitivity estimation through fitting procedure. Linear fit of the ellipticity transmission spectrum $\Delta\varepsilon(\lambda)$ of the clean sample (100 nm diameter Ni disk nanoantennas) in the vicinity of the null. Based on this experimental data set (λ step of 0.2 nm) the standard deviation σ for λ_ε is $1.0\text{x}10^{-4}$ nm. The inset shows the variation of σ for 6 $\Delta\varepsilon(\lambda)$ measurements of the clean sample taken in sequence before the MLD experiment. From these we obtain an average standard deviation $\sigma_{Ave} = 7.1\text{x}10^{-5}$ nm in the determination of λ_ε, which is about 7 times smaller than that of $5.0\text{x}10^{-4}$ nm reported in Supplementary Ref. [3] and about 3 times smaller than that reported in Supplementary Ref. [4] (in the latter case the standard deviation of the peak position is $1.8\text{-}2.0\text{x}10^{-4}$ nm from Fig. 3b of that manuscript). The standard deviation of these sequence of measurements, σ(σ) in the inset, also referred to as short-term noise level figure, in our case resulted in $4.4\text{x}10^{-5}$ nm to be compared to a value of $9.9\text{x}10^{-5}$ nm quoted in Supplementary Ref. [4]. This analysis demonstrates that even after a mathematical fit of the data, the higher sensitivity of our approach in comparison to the best values reported so far in literature, is confirmed.

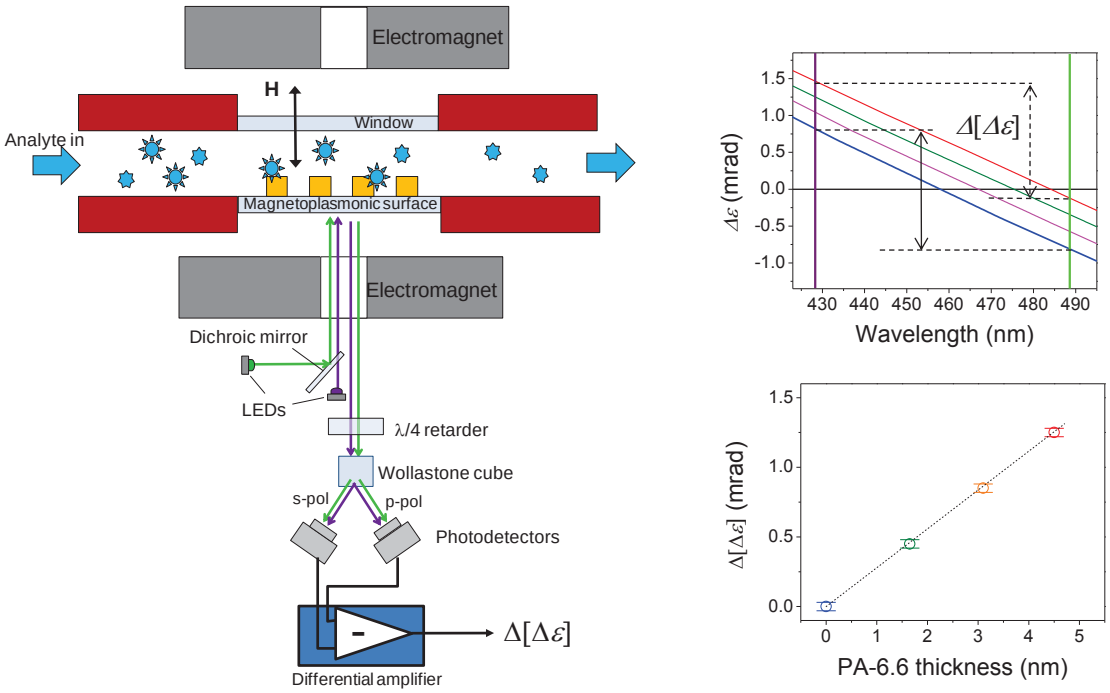

Supplementary Figure 6. Practical implementation of a detection scheme. The shift of the null wavelength λ_ε of the reflected light ellipticity ε caused by variations of the local refractive index can be precisely determined without the need of recording a full spectrum $\Delta\varepsilon\,(\lambda)$. The ellipticity spectra $\Delta\varepsilon\,(\lambda)$ of the clean sample and after a few cycles of PA-6.6 MLD (2, 4, and 6 cycles) discussed in the manuscript is shown. Using only two light wavelengths, one before and one after the zero-crossing of ε (violet and green vertical lines in the plot), which can be provided by two light emitting diodes (LEDs, as depicted in the schematic of the setup), the light intensity of the two LEDs or the photodetectors gain is adjusted to compensate the signal ($\Delta[\Delta\varepsilon] = 0$) for the clean sample. **c** As the zero-crossing wavelength λ_ε shifts upon nylon deposition, this causes $\Delta[\Delta\varepsilon]$ to become positive and proportional to the PA-6.6 thickness, as shown in the plot $\Delta[\Delta\varepsilon]$ vs. PA-6.6 thickness. The plot shows that given the typical error bars in the measurement of $\Delta\varepsilon$, sub-nm variations of PA-6.6 thickness are easily detectable in this simple way.

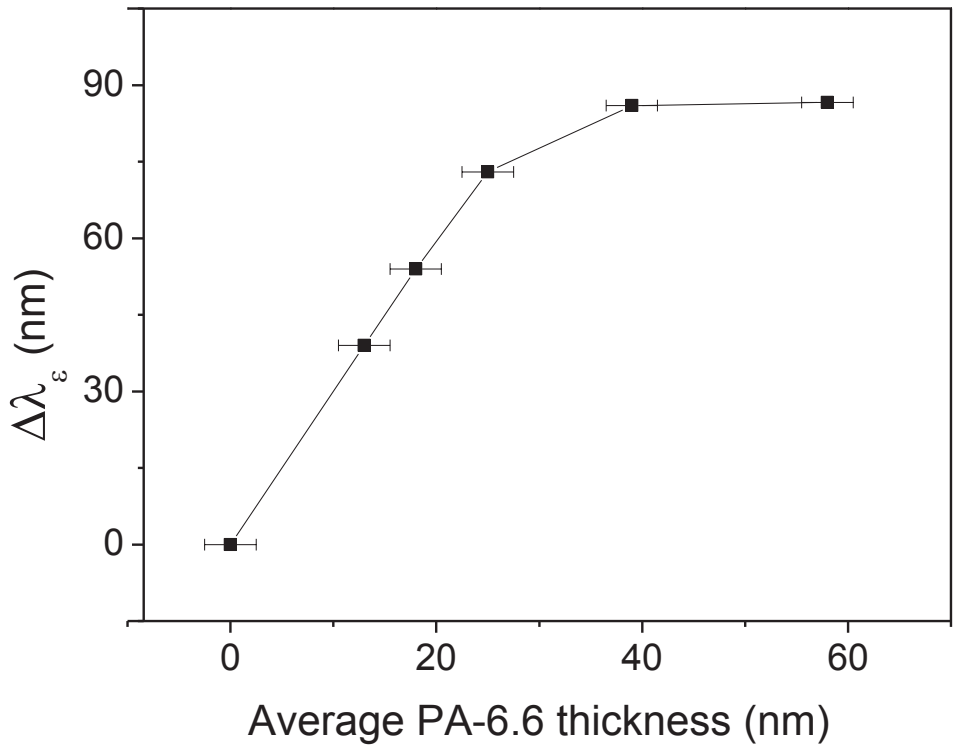

Supplementary Figure 7. Saturation of the shift of the Faraday ellipticity null-point. $\Delta\lambda_\varepsilon$ shift in transmission geometry of Ni nanodisks with D=100 nm and t=30 nm as a function of the PA-6.6 average thickness. The saturation of the effect happens at a thickness very close to the spatial extension of the electromagnetic near-field shown in Supplementary Fig. 4 (~35 nm). The total shift of the Faraday ellipticity null-point is the same of the LPR peak, viz. ~90nm. Both effects saturate after a shift of ~90nm.

SUPPLEMENTARY REFERENCES

[1] Vavassori, P. Polarization modulation technique for magneto-optical quantitative vector magnetometry *Appl. Phys. Lett.* **77**, 1605-1607 (2000).
[2] Maccaferri, N. et al. Polarizability and magnetoplasmonic properties of magnetic general nanoellipsoids *Opt. Express* **21**, 9875-9889 (2013).
[3] Dahlin, A.B., Tegenfeldt, J.O., & Höök, F. Improving the instrumental resolution of sensors based on localized surface plasmon resonance *Anal. Chem.* **78**, 4416-4423 (2006).
[4] Chen, S., Svedendahl, M., Käll, M., Gunnarsson, L., & Dmitriev, A. Ultrahigh sensitivity made simple: nanoplasmonic label-free biosensing with an extremely low limit-of-detection for bacterial and cancer diagnostics *Nanotechnology* **20**, 434015 (2009).